Titre: Title:	Combining dopamine and glucose sensings on paper devices for the metabolic study of neurosecretion
Auteurs: Authors:	Rémi François Dutheil, Dabeaurard Tho, Poulomsongo Iman Pitroipa, & Raphaël Trouillon
Date:	2025
Type:	Article de revue / Article
Référence: Citation:	Dutheil, R. F., Tho, D., Pitroipa, P. I., & Trouillon, R. (2025). Combining dopamine and glucose sensings on paper devices for the metabolic study of neurosecretion. Biosensors and Bioelectronics: X, 24, 100601 (12 pages). https://doi.org/10.1016/j.biosx.2025.100601

Titre de la revue: Journal Title:	Biosensors and Bioelectronics: X (vol. 24)
Maison d'édition: Publisher:	Elsevier, BV
URL officiel: Official URL:	https://doi.org/10.1016/j.biosx.2025.100601
Mention légale: Legal notice:	© 2025 The Authors. Published by Elsevier B.V. This is an open access article under the CC BY-NC-ND license (http://creativecommons.org/licenses/bync-nd/4.0/).

Biosensors and Bioelectronics: X 24 (2025) 100601

Contents lists available at ScienceDirect

Biosensors and Bioelectronics: X

journal homepage: www.journals.elsevier.com/biosensors-and-bioelectronics-x

Combining dopamine and glucose sensings on paper devices for the metabolic study of neurosecretion

Rémi F. Dutheil [a], Dabeaurard Tho [a], Iman Pitroipa [a], Raphaël Trouillon [a,b,c],*

[a] Department of Electrical Engineering, Polytechnique Montréal, 2500 chemin de Polytechnique, Montréal, H3T 1J4, Québec, Canada
[b] TransMedTech Institute, Montréal Québec, Canada
[c] SNC Research Group, Montréal Québec, Canada

ARTICLE INFO

Keywords:
Glucose
Dopamine
Paper devices
Electrochemistry
Enzymatic biosensors
Cell models

ABSTRACT

Glucose, the main source of energy of the human body, and dopamine, a major neurotransmitter, are two analytes widely investigated in the study of the brain. In many pathologies, a dysfunction in their metabolic pathways can be observed, leading to neurological disorders. Better understanding the interplays between secretion and cellular metabolism is critical to better address these diseases. In this study, we study the simultaneous detection of glucose consumption and dopamine secretion using a paper-based electrode (PBE). An electrode made of carbon nanotube-coated paper was functionalized with platinum nanoparticles and glucose oxidase to gain sensitivity towards glucose. Maximal current density (J_{max}) and Michaelis–Menten constant (K_m) were respectively 12.4 ± 2.0 μA.mm^{-2} and 7.6 ± 1.5 mM for the glucose calibration. The results suggest that dopamine secretion and glucose consumption can be measured in a neuron cell model using the developed paper-based sensor. After stimulating the cells, glucose and dopamine concentration decreased by 1.1 mM and increased by 7.1 μM, respectively. In addition, to confirm the sensor's detection of dopamine secretion, the impact of L-DOPA, a dopamine precursor, was tested. Dopamine secretion increased two-fold after incubation with L-DOPA, while glucose consumption remained unchanged. This opens new opportunities for quantitative, rapid multianalyte sensing of the chemical inputs and outputs of cellular mechanisms with an easy-to-use and affordable device.

1. Introduction

The brain is a crucial organ responsible for data analysis, processing and cognition. As a chemical object, its structure and functions are complex (Webster, 2001). The chemistry of the brain is still largely unknown, and better understanding the molecular interplays between its different components is paramount to elucidate its mechanisms and propose better treatments for the diseases of the brain. Neurotransmitters, a group of specialized signaling molecules, allow communication between neurons across their intercellular connections, called the synapse (Hyman, 2005). This mediation underlines the basic functions of the neuronal networks, and is also a pharmacological target. Dopamine (DA) is a major, well-studied neurotransmitter since its discovery by Arvid Carlsson in 1957 (Carlsson et al., 1957, 1958). A dysfunction in DA signaling has been found in several neurological and psychiatric disorders such as Parkinson's disease, schizophrenia, or deficit hyperactivity disorders (ADHD) (Marsden, 2006).

Importantly, and because of the high metabolic need of its constant cellular processing, the brain is the main glucose consumer in vertebrates (Vannucci and Vannucci, 2000; Dienel, 2019). D-glucose (GLC), the energy source of the Krebs cycle, is the predominant cerebral energy fuel and is therefore the principal analyte of interest to investigate metabolism, at the cell and organ levels. A dysfunction in GLC pathway is implicated in several diseases *e.g.* diabetes which was reported to touch 382 millions of people in 2013 (Zimmet et al., 2014). Pathological GLC metabolism in brain cells impairs the normal activity of neurons, which is highly correlated with neurodegenerative diseases (Han et al., 2021). Furthermore, after a traumatic brain injury, massive, repeated and synchronized depolarizations of neurons can be observed from the wound site, a phenomenon known as cortical spreading depolarizations (Jalloh et al., 2015; Rogers et al., 2013). These successive depolarization are followed by the re-establishment of the ion gradient across the neuron membrane, *i.e.* the repolarization of neuron, which is a highly energy-intensive process, leading to transient drops in GLC levels, and increases in blood flow and lactate levels, an anaerobic metabolic product (Rogers et al., 2013). This depletion of brain GLC is highly correlated with poor prognosis, thus supporting the

---

* Corresponding author at: Department of Electrical Engineering, Polytechnique Montréal, 2500 chemin de Polytechnique, Montréal, H3T 1J4, Québec, Canada.
E-mail address: raphael.trouillon@polymtl.ca (R. Trouillon).

https://doi.org/10.1016/j.biosx.2025.100601
Received 31 July 2024; Received in revised form 14 February 2025; Accepted 6 March 2025

importance of better understanding the relationships between neuronal activity and metabolism (Rogers et al., 2013; Vespa et al., 2003).

Over the last decades, several methods and technologies have been developed for the analysis of brain chemistry. Colorimetric and fluorometric detections offer easy-to-use and versatile approaches for biosensing devices, but their low time resolution and quantitative capabilities limit their applications (Neubauerova et al., 2020). Currently, several methods for GLC analysis exist, based on different technologies such as high-performance liquid chromatography (HPLC), capillary zone electrophoresis and optical spectroscopy (Lee et al., 2019; Taguchi et al., 2003; Sun et al., 2018). Despite the advantages of these methods, they are expensive, require trained personnel and complex sample preparation, such as purification (Lee et al., 2019). Electroanalytical methods were suggested in the 1970s for small brain molecules detection by Ralph Adams (Adams, 1976). Firstly used for neurotransmitter detection (Simonsson et al., 2012), this quantitative approach has been since developed to detect several molecules such as DNA and enzymes *ex vivo* and *in vivo* (Bouffier et al., 2021). It is now fully integrated into the field of biosensor for fast quantitative chemical measurements in living and artificial samples, especially in the brain (Smith et al., 2018). For instance, cyclic voltammetry (CV) can be used for the detection of biomolecules, such ase DA and GLC (Bai et al., 2008; Raj et al., 2003; Zachek et al., 2008). The material and the geometry of the sensor can impact the sensitivity of this type of devices (Bard et al., 2022; Trouillon and Gijs, 2018; Pelletier and Trouillon, 2024; Trouillon et al., 2010). Each redox couple produce a specific shape of voltammograms, which allows the selective identification of electroactive species based on their peak potentials and the curve of their CV. The environment, the electrode surface quality and the species of interest are all important features impacting the electrochemical signal (Michael and Borland, 2006). The rise of electrochemical biosensors led to the development of enzymatic GLC biosensors (Wang, 2008). Based on glucose oxidase (GOx), these devices use the specificity of the enzymatic reaction to detect GLC which is typically hard to detect with an unmodified electrode. However, the fabrication process of electrochemical sensors and their use can be complex and expensive. New technologies were developed to answer the need for simpler and cheaper electrochemistry devices.

Paper-based electrodes (PBE) offer an affordable, easy-to-use and -fabricate technical solution for the detection of multiple metabolites (Ozer et al., 2020; Martinez et al., 2007; Trouillon and Gijs, 2018; Pelletier and Trouillon, 2024). Initially developed by Whitesides' research team in the early 2000's, this low resource environment device can be upgraded with electronics, 2D and 3D printing and microfluidics systems to address a wide range of applications (Bruzewicz et al., 2008; Martinez et al., 2007). It is possible to build electrochemical sensors from PBE (Trouillon and Gijs, 2018; Pelletier and Trouillon, 2024; Cate et al., 2015; Trouillon and Gijs, 2023). In comparison to the traditional flat electrode surfaces, the 3D structure of paper electrodes is also expected to reduce the fouling of the device (Trouillon and Gijs, 2018). Its biocompatibility allows the culture of cells in the pores of paper, mostly in a well-chosen extracellular matrix (ECM) biogel (Derda et al., 2009). This offers the opportunity to combine a paper-based sensor with cell culture (Trouillon and Gijs, 2023; Ali and Trouillon, 2024). The shape, surface treatment and conductive electrode coating applied on the PBE can be customized for a specific application (Pelletier and Trouillon, 2024; Liu et al., 2016). Carbon nanotubes (CNT) as an electrode material have shown great electrochemical activities, high electrode stability and resistance to fouling effect (Pumera, 2009; Gooding, 2005). PBE can provide results comparable to HPLC with an easily disseminated technology (Cate et al., 2015). By combining two or more working electrodes, PBE can simultaneously also detect multiple metabolites and biomarkers (Dossi et al., 2013).

In this article, the co-detection of GLC and DA with PBE is presented. A GLC-sensing chemistry based on GOx immobilization on a PBE decorated with Pt nanoparticles (NP) is described and used in a model of neurometabolic analysis. The sensor device was characterized with scanning electron microscopy (SEM) and X-ray photoelectron scattering (XPS). The basic electrochemical properties of the devices were investigated with GLC and DA alone, and combined to obtain single or bi-analyte calibration curves. Next, GLC consumption and DA secretion in PC12 cells cultured directly in the pores of the paper were quantified, and the impact of L-DOPA, a DA precursor, was investigated.

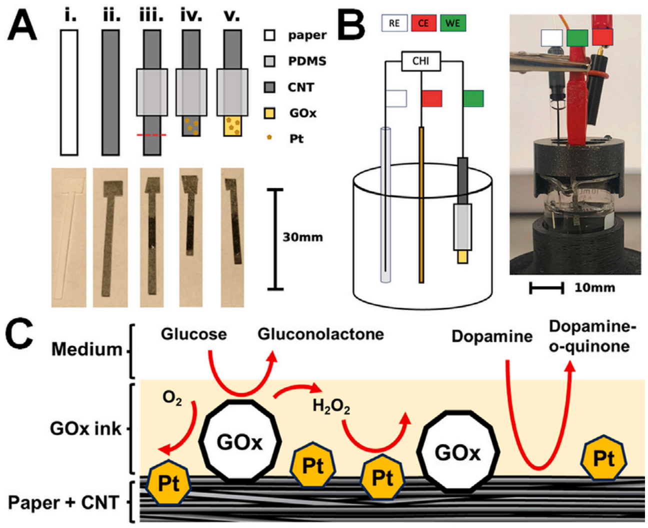

Fig. 1. Paper-based biosensor fabrication process, experimental set-up and reaction. (A) Electrode fabrication: i. Laser cutting of the electrodes (30 mm long, 1.9 mm wide); ii. Deposition of 5 layers of CNT ink; iii. PDMS deposition in a central part of the electrodeand active part cutting to 2-mm long; iv. Pt particles and v. GOx deposition. (B) Schematic and picture of a 3-electrode set-up with the working electrode (WE, green), reference electrode (RE, white) and counter electrode (CE, red). (C) Schematic of the GLC and DA detection reactions at the biosensor surface, as the H_2O_2 produced by the immobilized GOx from GLC is detected by the Pt NP decorating the PBE.

2. Materials and methods

2.1. Reactants and solutions

All the reactants were purchased from Millipore-Sigma (Canada), unless specified otherwise. Deionized water (resistivity > 18 MOhm cm) was used for preparing all the solutions. The solution for Pt NP deposition was 1 mM of $H_2PtCl_6.6H_2O$ in 0.1 M KCl. The CNT commercial solution was used as received (single-walled CNT, SWCNT, in water, 0.2 mg mL^{-1}, with sodium dodecyl sulfate, SDS, to stabilize the suspension). 1 mM DA hydrochloride in PBS (pH = 7.4) solutions were prepared daily. D-(+)-GLC was diluted in PBS to make GLC stock.

GOx enzyme from *Aspergillus niger* was purchased from Millipore Sigma Canada (100–250 units per mg, reference G7141). The final enzyme solution used for biosensor preparation contained 60 mg mL^{-1} GOx (otherwise stored at −20 °C as a powder), 30 mg mL^{-1} bovine serum albumin (BSA), 60 mg mL^{-1} poly-(ethylene glycol)-diglycidyl ether and 1% glycerol in phosphate buffered saline solution (PBS 0.01 M, pH 7.4).

2.2. Electrodes fabrication

This method was adapted from a published protocol (Trouillon and Gijs, 2018). First, Whatman grade 1 filter paper (thickness 180-μm, pore size 11-μm) was laser cut into strips (1.9-mm wide, 30-mm long) with a Rayjet 50 laser cutter, as presented in (Fig. 1.A.i.). This strip shape was designed to reduce the electrode resistance and improve the electrochemical behavior of the active part of the electrode (Trouillon and Gijs, 2018; Pelletier and Trouillon, 2024). The paper pieces were cleaned by sonication for 180 s in isopropanol and water, successively, and dried for 5 min at 90 °C in the oven. The cleaned paper strips were dipped in the carbon nanotubes (CNT) solution and cured in the oven at 90 °C for 5 min. This step is repeated 4 times to deposit 5 layers of CNT overall. The goal is to build a thicker CNT layer and improve the electrode conductivity of the paper strips (Fig. 1.A.ii) (Pelletier and Trouillon, 2024). Next, the central section of the paper electrodes was blocked with polydimethylsiloxane (PDMS) to prevent complete soaking of the sample by capillarity once the electrode is placed in contact with a solution (Fig. 1.A.iii). Briefly, PDMS (prepared in a 10:1 mix ratio) is painted with a brush into the two faces of the paper strip and polymerized in the oven at 90 °C during 2 h. One end of the strip was cut to form a 2-mm (measured from the PDMS interface) by 1.9-mm sensing site (active part).

2.3. Electrodes functionalization with GOx

To make the PBE sensitive to H_2O_2, which is the product of the GOx enzymatic reaction allowing for GLC detection, Pt NP were deposited on the sensing site of the paper electrode (Fig. 1.A.iv). Briefly, the active part of the electrode was dipped in 1 mM of $H_2PtCl_6.6H_2O$ in 0.1 M of KCl. Different potential steps were applied with a potentiostat CHI 1040 (CH Instruments, Inc). Two potential controls were tested. First, a two steps deposition (M2), with a potential of −1 V applied during 9 s followed by 1 s at 1 V. Secondly, a three steps deposition named M3, with a first step at −1 V during 9 s, followed by 10 s at 0 V and 1 s at 1 V. For M2 and M3, Pt deposition was tested with 30 or 50 cycles.

Then, the GOx enzymes were encapsulated on the sensing part of a Pt-NP-modified PBE (Fig. 1.A.v). The purpose is to build a first-generation GLC sensors, where the GOx-mediated GLC oxidation is combined with the production of H_2O_2 that can be detected at the Pt NP. After the Pt NP deposition, the electrode was dipped during 10 s in a GOx ink consisting of GOx (from *Aspergillus niger*, 100,000–250,000 units/g, 60 mg mL^{-1}), bovine serum albumin (BSA, 30 mg mL^{-1}), poly-(ethylene glycol)-diglycidyl ether (60 mg mL^{-1}) and 1% v/v glycerol in PBS. Following the GOx deposition step, the electrode was dried during 2 h at 50 °C following a previously published protocol (Knudsen et al., 2023; Trouillon et al., 2017; Vasylieva et al., 2011). In agreement with the literature, the drying temperature was chosen to be in the optimum range temperature of 40–60 °C, but without exceeding the limit of 50 °C to avoid the risk of enzyme denaturation (Mandpe et al., 2020; Khatami et al., 2022; Bankar et al., 2009).

For the XPS analyses, and to confirm the presence of GOx on the electrode, a similar ink without GOx was prepared. This was done by replacing the GOx by the same amount of BSA: BSA (90 mg mL^{-1}), poly-(ethylene glycol)-diglycidyl ether (60 mg mL^{-1}) and 1% v/v glycerol in PBS. The rest of the functionalization protocol was unchanged.

2.4. SEM and XPS analysis

A Quattro ESEM microscope was used for the SEM analysis, with charge compensation and a pressure in the chamber at 100 Pa. The high voltage is set at 10 kV. Three different areas of the PBE were investigated (see Figure S1.A. in Supplementary Information): (i) on the electrode body, above the PDMS deposition (area A, Figure S1.B.), (ii) near the PDMS area in the sensing part of the electrode (area B, Figure S1.B.) and (iii) at 1 mm in the middle of the active part (area C, Figure S1.B.). Once SEM images were obtained, ImageJ (Schneider et al., 2012) was used to measure the surface covered by the Pt NP, their size and density. Each SEM image was split in at least 4 different parts, analyzed separately.

A VG ESCALAB 250Xi photoelectron spectrometer placed in a vacuum chamber was used for the XPS analysis, with charge compensation. The source is a Mono Al Kα 1486.68 eV. The depth analyzed was 10 nm on a surface of 1 mm of diameter. Charge correction was performed by placing the C 1s peak at 284.6 eV. Samples were adhered to the sample holder with conductive tape and analyzed using the standard XPS charge compensation. Spectra were analyzed with Avantage v6.5. All high-resolution spectra were decomposed into symmetrical components of Lorentzian/Gaussian functions, with the exception of the C1s component relating to the sp2 carbon in CNT, which is asymmetrical. The asymmetry parameters were optimized to obtain results consistent with the concentrations of oxygen-containing groups. The same asymmetry parameters were used for all samples containing CNTs.

2.5. Electrochemical analysis

CV were run with a CHI 1040C (CHInstrument, USA). The potentiostat was connected to a 3-electrode set-up with the paper electrode as the working electrode (WE), a Pt wire for the counter electrode (CE) and an Ag|AgCl (3 M NaCl) electrode for the reference electrode (RE) as presented in (Fig. 1.B). All the potentials are reported *vs.* Ag|AgCl (3 M NaCl). The scan rate (SR) used was 50 mV s^{-1}, and the potential range was from −0.9 V to 0.9 V. For similar PBE, the first scan was found to be prone to high variations, especially in biological conditions, as the electrode stabilizes (Trouillon and Gijs, 2018; Pelletier and Trouillon, 2024). As a result, three CV cycles were applied for each measurement. Only the third CV cycle was used for the analysis. As discussed below, several CV features were considered. The current density J was obtained by normalizing the current magnitude of the peaks with the surface of the sensing part of the electrode (Bard et al., 2022). The surface of the sensing part was measured with digital calipers: the length on both side on the active part of the electrode were multiplied by the width (1.9-mm). The current density allowed to control for the variations in electrode lengths and their impact on the electrochemical signal.

The characterization of the sensor without GOx was performed in a solution of 1 mM hexaammineruthenium(III) chloride (RuHex) in 1 M KCl. A range from 30 to 100 mV s^{-1} of scan rate (SR) were applied and CV were compared. For each SR tested, the redox peak separation (ΔE) and the height of the reduction peak were compared. The double layer capacitance C_{dl} was deduced from the charging current (i_c) measured at a potential of −0.3 V. Four different electrodes were used (n = 4).

2.6. Calibration data analysis

The vertex height at 0.9 V was measured for different [GLC] and/or [DA]. This calibration was done for the paper-based sensor with and without GOx. For each pair of [GLC] and [DA], the current measured is normalized by the size of the active part of the electrode, so the current density J is represented as a function of [GLC] or [DA]. Ranges from 0 to 30 mM and from 0 to 50 μM were investigated for GLC and DA, respectively. For each condition of the sensor (with/without GOx), a 3D surface was fitted to this calibration data using polynomial regression in Python. Finally, the calibration surfaces with or without GOx were normalized by removing the current density at the condition (GLC = 0 mM, DA = 0 μM). For each condition of DA and GLC investigated, at least 4 different electrodes were tested, and the current density J reported is their mean ± standard deviation (SD).

2.7. Cell culture

PC12 cells, a model of dopaminergic neurons originating from the rat pheochromocytoma, were cultured in RPMI-1640 medium supplemented with 0.4% penicillin-streptomycin, 5% of fetal bovine serum (FBS), 10% horse serum (HS), and 2 mM of glutamine. The cells were passaged every week in a 1:5 ratio and resuspended in fresh medium. Otherwise, the medium was changed every other day. PC12 cells were cultured for 20 passages. For the cells experiments, and to integrate the cells in the PBE, 0.5 million PC12 cells in 2 μL of Engelbreth-Holm-Swarm murine sarcoma extracellular (ECM) gel were deposited

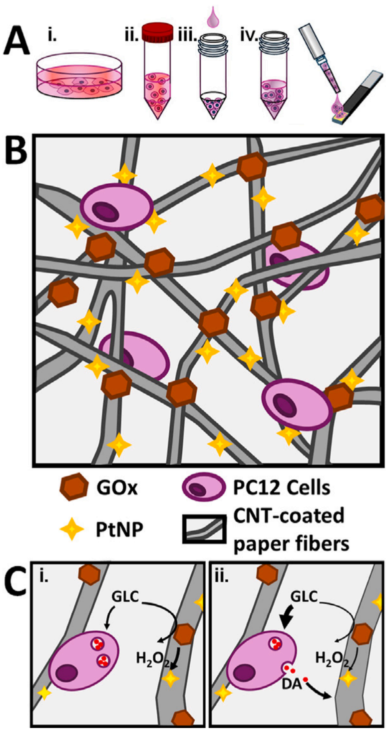

Fig. 2. Preparation protocol for the cell-based experiments. (A) Protocol for depositing PC12 cells on the PBE: i- Cell culture in medium. ii- Cell collection. iii- Centrifugation and removal of the culture medium. iv- Suspension in ECM gel, with 0.25 million cells per μL. v- Deposition of 2 μL (with 0.5 million cells) on the sensing part of the sensor. (B) Schematics of the assembled PBE with PC12 cells maintained in the pores of the paper and featuring the different parts of the sensor. (C) Detection reactions i- before and ii- during cell activation. In the absence of stimulation (i.), the extracellular levels of GLC corresponding to baseline PC12 metabolism status are detected with the PBE. After ACh stimulation (ii.), PC12 cells will secrete DA that will then be detected by the PBE. As the cells are active, they consume more GLC, thus reducing the substrate availability for GOx reaction and the associated GLC signal.

on the sensing part of the electrode, as presented in Fig. 2.A. This was done by centrifugating the cells at 1000 RPM for 5 min, removing the supernatant and resuspending them in a well-chosen volume of gel. After deposition, the ECM gel was allowed to set during 5 min in the humid incubator at 37 °C and incubate in PC12 medium until use of the device. Before each experiment, the active part of the sensor with cell was incubated during 3 min in 5 mM GLC in PBS, as the first experiment condition.

Three conditions were investigated for the cells experiments. For all conditions, a first CV was run in 5 mM of GLC in PBS at $t = 0$ s, following by an incubation time of 200 s and a second CV run at $t = 200$ s. For the ‘control’ condition, the second CV was obtained in a solution of GLC at 5 mM in PBS. For the stimulated condition, named ‘ACh’, PC12 cells were stimulated with 100 μM of acetylcholine chloride (ACh) in 5 mM GLC in PBS during 200 s. This high ACh concentration was used to ensure that all cells are stimulated, without being a limiting factor for the dopamine secretion. It has been reported to induce a maximal level of exocytosis for the electrochemical detection of DA (Shinohara et al., 2008). Next, the CV were measured after the 200 s incubation time. For the third condition named ‘L-DOPA’, the PC12 cells, maintained in the PBE, were incubated during 1 h in culture medium with 100 μM of L-3,4-dihydroxyphenylalanine (L-DOPA), and CVs at t = 0 s and t = 200 s were obtained following the ‘ACh’ protocol presented above. As summarized in Fig. 2.B and C, it is expected that ACh exposure will lead to DA secretion, that can be detected by the CNT part of the PBE. Simultaneously, the high level of metabolism induced by the ACh stimulation will lead to GLC consumption by the cells and possibly to an overall drop in [GLC] in the sample. This should be also detected by the GOx-functionalized PBE. All the solutions were kept at 37 °C.

For all these conditions, the vertex height at 0.9 V was measured. This current was next normalized by the size of the active part of the electrode to obtain J. Then, $J_{(t=200\ s)}$ was used to determine $\Delta J_i = J_i - J_{control}$, with (i) the condition ACh or L-DOPA. The median, first and third quartile were calculated for ΔJ_i and J_i at t = 200 s and used to compare results between the different groups.

2.8. Fluorescence microscopy

PC12 cells were incubated and deposited in the PBE following the protocol for the cell-based experiments (Fig. 2.A). After allowing the ECM gel to set, cells were fixed in 3.7% methanol-free formaldehyde solution in PBS for 15 min at room temperature. Next, the cell membranes were permeabilized in 0.1% Triton™ X-100 in PBS for 15 min, and the PBE were next incubated during 40 min with Alexa Fluor™ 488 Phalloidin (ThermoFisher). Finally, the samples were maked with SYTOX™ Deep Red Nucleic Acid Stain (ThermoFisher) during 30 min. Between all these steps, samples were washed twice in pre-warmed (37 °C) PBS.

After staining, the cells were imaged with a Nikon Eclipse TiE inverted C2 epifluorescence microscope fitted with a 20X objective, and z-stacks were acquired. ImageJ was used to process the micrographs. To better observe the paper geometry, differential interference contrast (DIC) was used to image the general topology of the sample. The DIC image was inverted and is here reported in blue to highlight the position of the paper fiber. The contrast of the images was modified to better show the position of the cells in the paper fibers.

2.9. Statistical analysis

All data were tested to follow a gaussian distribution using Shapiro tests. For data following a gaussian distribution, results are presented as mean ± standard deviation (SD), and statistical analysis was conducted with a ANOVA single factor test. For nonparametric data, a Mann–Whitney U test is performed to compare median between all the experiments and results are presented as median with interquartile range (IQR, 1st quartile – 3rd quartile).

3. Results and discussion

3.1. Pt nanoparticle deposition on paper electrodes

Different Pt NP deposition techniques were considered, namely the M2 or M3 steps potential deposition. The parameters of one cycle of the multistep protocols, along with the associated electrochemical currents, are shown in Fig. 3.A and 3.B. Each of these cycles was repeated 30 or 50 times. During the −1 V phase, the Pt ions are reduced, thus building the Pt NP. A short pulse at 1 V was also added to stabilize the particles and homogenize their size. As the paper is a porous material, a constant Pt deposition is expected to rapidly deplete the samples of Pt ions, thus reducing the size of the NP. To mitigate this, in the 3 step-method (M3), we have added a 0 V step for 10 s. This step was designed to help replenish the electrode vicinity with Pt ions and improve NP deposition.

SEM analysis was carried out to investigate the impact of these different conditions on the characteristics of the electrodeposited Pt NP (Fig. 3.C). Three features were analyzed: the percentage of electrode surface covered by Pt, the size (Fig. 3.D) and density (Fig. 3.E) of the Pt NP. The Table 1 summarizes these data for an area of the sensing part close to the PDMS layer. Figure S1.B and Table S1 in the supplementary material presents similar data for a zone at 1 mm of the PDMS layer in the sensing part of PBE (Figure S1.A, zone C).

Overall, the three step deposition M3 led to higher surface coverage of Pt NPs, with 10.92% and 43.97% respectively for 30 and 50 deposition cycles, in comparison to the M2 method, with 0.66% and 1.12% (for 30 and 50 deposition cycles, respectively).

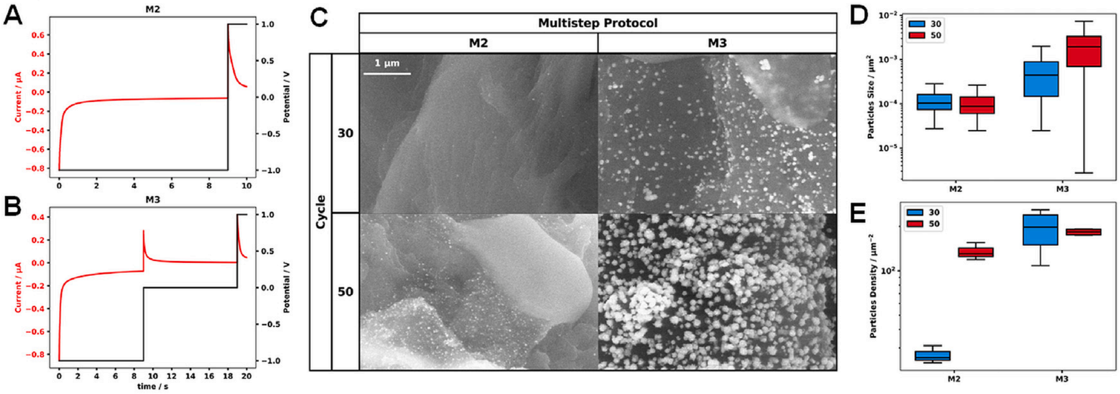

Fig. 3. Multistep protocol applied for Pt NP depositions (A- M2 and B- M3). C) Typical SEM images of PBE decorated with Pt NP for two NP deposition technique (M2: two steps ; M3: three steps) and for 30 or 50 cycles. Pt NP characterization. D) Pt NP size and E) density, for each Pt deposition condition.

Table 1
Surface Covered by Pt nanoparticles, nanoparticles size and density analyzed by SEM.

Method	M2		M3	
Cycles	30	50	30	50
Surface Covered (%)	0.66	1.12	10.92	44.48
Particles Size (10^{-5} µm^2) (median (IQR))	10.45 (7.43-16.23)	8.80 (6.05-14.3)	44.97$^{\#\#\#}$ (14.72-89.31)	193.5$^{\#\#\#,***}$ (69.86-334.03)
Particles density (µm^{-2}) (mean ± SD)	26.85 ± 3.75	134.97*** ± 18.49	190.88$^{\#\#}$ ± 68.10	183.23$^{\#\#}$ ± 9.66

IQR: interquartile range. Data from a same multi-step method (M2 or M3 respectively) are compared with a Mann–Whitney U test for particle density and ANOVA for particle Density (*: p<0.05, **:p<0.01, ***: p<0.001). Data for a same number of cycles applied (30 or 50 respectively) are compared with a Mann–Whitney U test for particles density and ANOVA for particles Density ($^{\#}$: p<0.05, $^{\#\#}$: p<0.01, $^{\#\#\#}$: p<0.001).

Furthermore, the Pt NP obtained from M3 are significantly bigger than from the M2 multistep method for both 30 and 50 cycles of deposition ($p < 0.001$). The size of Pt NP for 50 cycles is also higher than for 30 cycles ($p < 0.001$) when a 3-step multistep deposition M3 was applied. There was no significant difference between 30 and 50 cycles for the M2 method. Moreover, the M3 method led to a higher particles density *vs.* M2, for both 30 and 50 deposition cycles ($p < 0.001$). Increasing the number of cycles to 50 cycles was also found to increase significantly the particles density for M2 ($p < 0.001$), but no difference is observed with M3. This hints that the M3 approach allows for optimal nucleation of the NP, and the number of cycles allows for controlling the size. In contrast, as the density increases with the number of cycles for M2, the nucleation step is less efficient. This highlights the importance of the 0 V resting time added in M3, allowing for the relaxation of the diffusion profile and better mass transport in the recesses of the porous PBE.

Overall, the 3-step Pt deposition M3 produces the largest Pt NP with the highest density. Importantly, this optimization also translates to improved electrochemical H_2O_2 detection, and thus GLC as H_2O_2 is an enzymatic reporter of GLC oxidation by GOx. Voltammograms run in different H_2O_2 concentrations for different Pt NP preparations are shown in Figure S2. These results confirm that i- increasing the number or size of particles with more deposition cycles and ii- using the 3-step (*vs.* the 2-step one) approach both improve the electrode signal. The M3-50 protocol was used for the Pt deposition step in the electrode manufacturing process.

3.2. XPS analysis of the paper GLC sensors

XPS analyses were performed to study the chemical composition at the electrode surface for different steps of the fabrication process. Fig. 4 recapitulates the XPS spectra of four different electrode samples, with a focus on specific peaks highlighting their chemical modifications (Pt peak or C peak). Fig. 4.A and 4.B represent the XPS spectrum of paper electrode with CNT ink only (5 layers). A large C=C peak is observed, indicative of the presence of CNT. After Pt NP deposition (Fig. 4.C and 4.D), Pt is detected with 2 well-defined peaks between 70 and 80 eV.

Comparison between the spectra obtained for the BSA (Fig. 4.E and 4.F) and GOx (Fig. 4.G and 4.H) inks allows for confirming the presence of GOx in the enzyme layer. The BSA ink is here used only to mimic the presence of a high protein content layer on the sample. In contrast to the BSA ink sample, new carbon interaction are detected for the GOx ink, specifically peaks associated to amine C-N and amide O=C-N groups from the enzyme. This confirms that the GOx enzyme was successfully bound to the surface and retained some of its structure.

3.3. Electrode electrochemical characterization

Fig. 5.A shows typical CVs obtained in 1 mM RuHex in 1 M KCl for different SR (from 30 to 100 mV.s^{-1}) with the PBE with the Pt NP but without the GOx enzyme. For all the SR considered, a clear redox behavior is observed. However, as SR increases, the CVs get more distorted. In particular, the rise in peak separation for this outer-sphere redox species is indicative of low electrode conductivity leading to ohmic drop in the thin conductive layer of CNT deposited on the insulating cellulose paper (Trouillon and Gijs, 2018; Bertoncello et al., 2007). This can be mitigated by using lower SR, or reducing the size of the electrode. The electrode size was set at 1.9 mm × 2 mm, and the SR was set at 50 mV.s^{-1} for the rest for the study. The double layer capacitance C_{dl} (Fig. 5.B) was computed by measuring the charging current i_c at −0.3 V and dividing it by twice the SR, as presented in Eq. (1) (Bard et al., 2022):

$$C_{dl} = \frac{i_c}{2\ SR} \tag{1}$$

The peak separation ΔE between the anodic and cathodic peaks were measured and are reported in Fig. 5.C. The ΔE increases linearly with $SR^{1/2}$. As for an outer-sphere redox couple like RuHex, a reversible

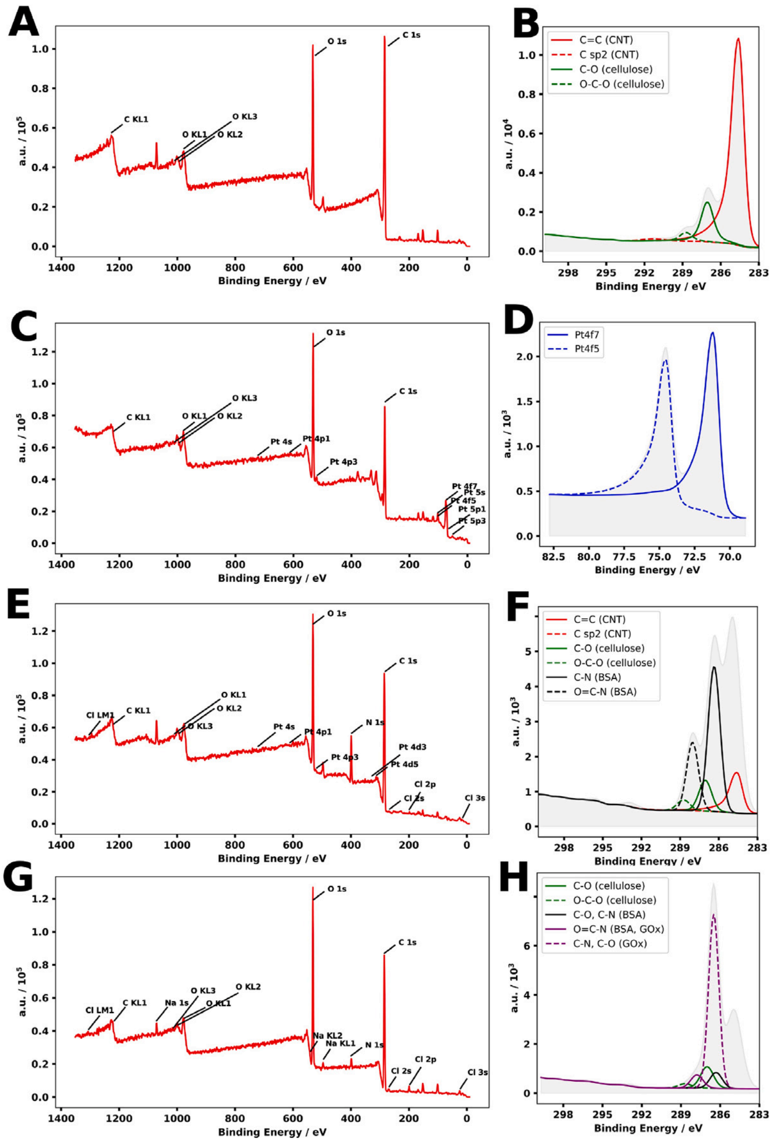

Fig. 4. XPS analysis of different paper-based sensors. XPS spectra for (A) paper electrode with CNT (with (B) focus on the C1s peak), (C) paper electrode with CNT and Pt NP (with (D) focus on the Pt peak in the XPS spectrum), (E) paper electrode with CNT, Pt NP and BSA layer (with (F) focus on the C1s peak), (G) paper-based biosensor with CNT, Pt NP and the GOx enzyme layer (with (H) focus on the C1s peak).

reaction is expected, this value should be closer to 60-70 mV according to the electrochemical theory. As discussed above, this was attributed to the electrical behavior of the electrode, where the thin CNT layer acting as the conductive layer is quite resistive (Trouillon and Gijs, 2018; Bertoncello et al., 2007). This leads to an ohmic drop along the length of the PBE and increased peak separation as SR increases.

The cathodic current density J of the reduction peak is reported in Fig. 5.D *vs.* $SR^{1/2}$. A linear relationship was found to adequately describe these variations. According to the electrochemical theory, this agrees well with a diffusive system, hinting that at these SR diffusion is not significantly hindered by the porous nature of the PBE (Bard et al., 2022; Scholz et al., 2010).

3.4. Calibration of the biosensor for GLC

The GOx-modified PBE were calibrated against GLC using CVs. Typical CVs are presented in Fig. 6.A. Several variations are observed as [GLC] changes but were not all found to be reliable indicators of [GLC]. For instance, the reduction peak at a potential close to −0.5 V was considered, but the current density variations measured in this way were not stable. The most reliable and sensitive feature was found to be the rise in anodic current recorded above 0.4 V. To facilitate the analysis, and overcome some of the variability amongst the different PBE, the current recorded at the positive vertex (here, 0.9 V) was used for GLC sensing. This is important to identify a robust electrochemical marker for our analysis, as biological measurements are typically carried out in a complex chemical background. Therefore, relying on a feature that can be quantified and processed easily, here the positive vertex, is expected to improve the stability of the measurements.

A calibration curve, processed from the data obtained from PBE GLC-sensors ($n = 8$ electrodes), is presented in Fig. 6.B. The background J recorded for [GLC] = 0 mM was subtracted from all the recorded J to focus on the variations induced by alterations in GLC levels. The current density dependence on [GLC] appears linear below 5 mM, and then starts reaching a plateau at higher concentrations as the enzymes saturate. This behavior is typical of enzyme sensors, and can be described by different theories. Here, the data was fit to a Michaelis–Menten model to extract the calibration parameters (Trouillon et al., 2017; Johnson and Goody, 2011; Michaelis et al., 1913):

$$J = J_{max} \frac{c}{c + K} \tag{2}$$

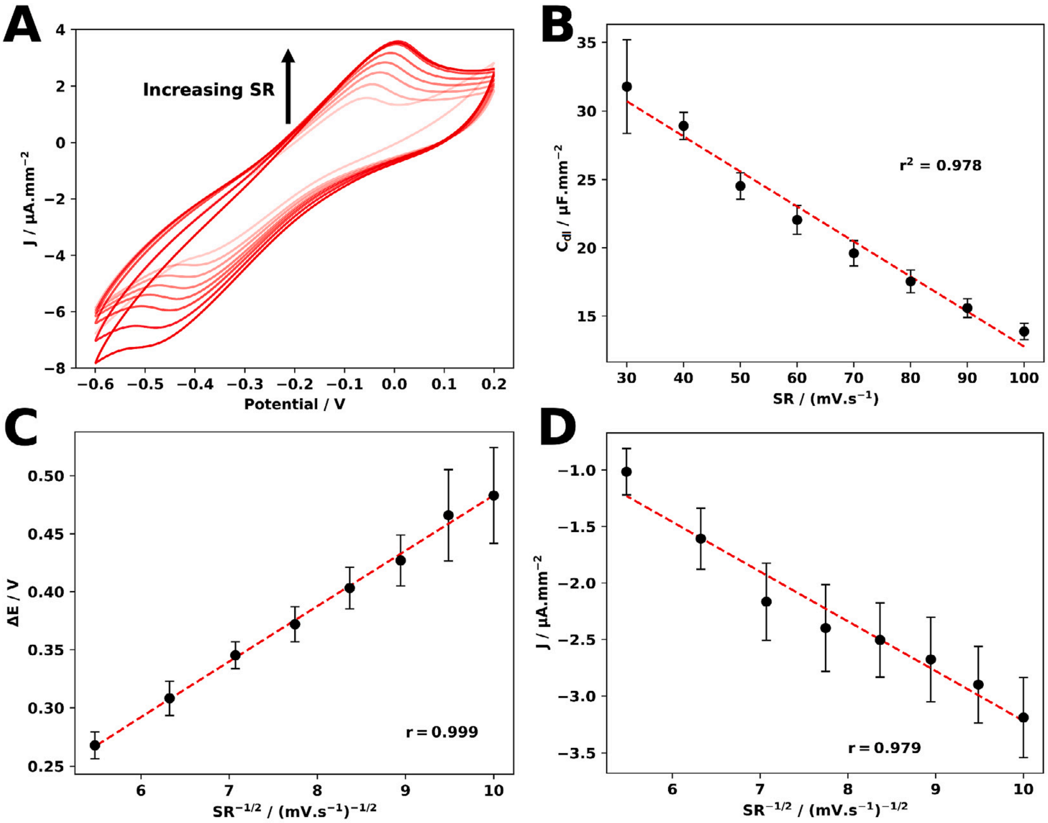

Fig. 5. Paper-based sensor behavior in 1 mM RuHex in 1M KCl. (A) Typical CV for SR from 30 to 100 mV.s^{-1}. Graphs showing the variations of the (B) double layer capacitance C_{dl} as a function of SR and (C) the peak separation ΔE and (D) the current density J as functions of SR$^{1/2}$ (n = 4, average ± SD).

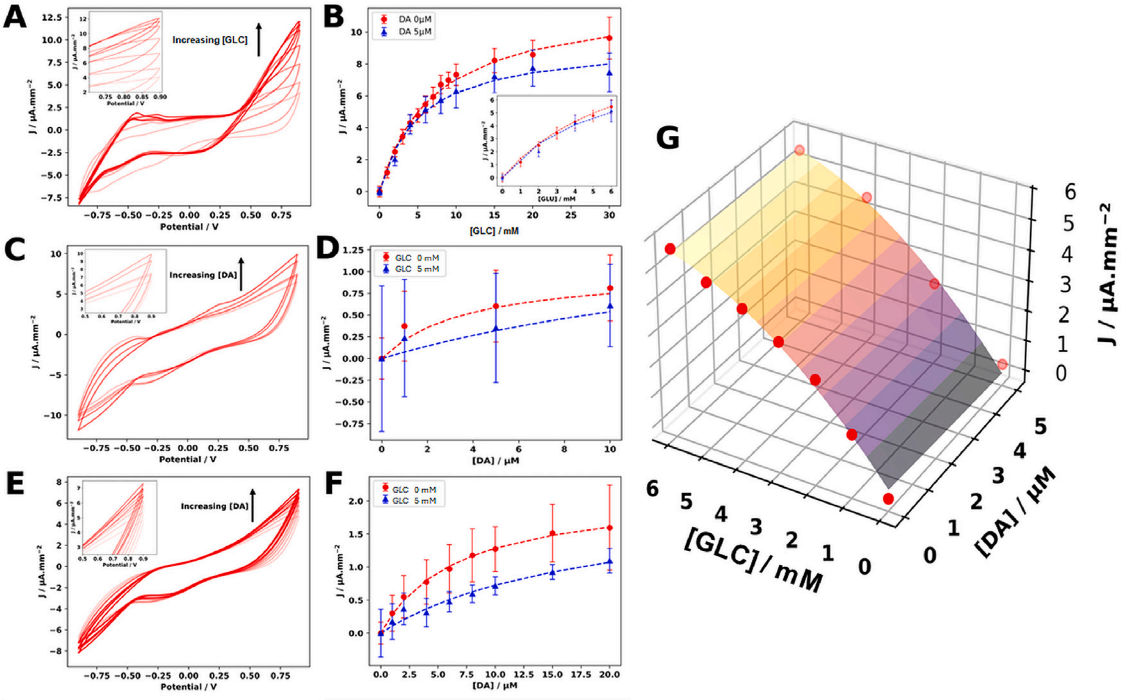

Fig. 6. Calibration curves for DA and GLC. (A) CVs with increasing [GLC] (no DA) for a GOx-modified PBE. (B) Calibration curve for GLC, with (n = 4) and without (n = 8) 5 µM of DA, with a GOx-modified PBE. (C) CVs for increasing [DA] (no GLC) and with GOx. (D) Calibration curve of DA, with (n = 3) and without (n = 4) 5 mM of GLC, with GOx-modified PBE. (E) CVs obtained for increasing [DA] (no GLC) for an electrode without the GOx ink deposition (only CNT and Pt NP). (F) Calibration curve of DA, with (n = 4) and without (n = 6) 5 mM of GLC, for an electrode without the GOx ink deposition (only CNT and Pt NP). (G) 3D surface for the dual GLC and DA calibration, with a GOx-modified PBE.

Table 2

Constants J_{max} and K for the GLC and DA calibration data (mean ± SD).

	GLC calibration		DA calibration			
	GOx		GOx		No GOx	
	DA = 0 μM	DA = 5 μM	GLC = 0 mM	GLC = 5 mM	GLC = 0 mM	GLC = 5 mM
J_{max}/μA mm^{-2}	12.382 ± 2.036	8.917 ± 1.713*	0.754 ± 0.148	0.516 ± 0.143	2.336 ± 0.983	2.013 ± 1.042
K/mM	7.581± 1.540	4.578± 2.292*	1.537 10^{-3}± 1.213 10^{-3}	1.132 10^{-3}± 0.29 10^{-3}	8.109 10^{-3}± 5.009 10^{-3}	19.549 10^{-3}± 9.08 10^{-3}
n	8	4	4	3	6	4

For each calibration, the fitted values obtained for J_{max} and K for the different conditions were compared for the presence or absence of 5 mM of the interfering molecules (DA or GLC) with an ANOVA test following confirmation of a Gaussian distribution with a Shapiro test (*: $p<0.05$).

where J_{max} is the maximum saturation current density, c the concentration and K is a concentration where the recorded J is half J_{max}. The parameters computed from this fitting are reported in Table 2 and were used to compare different conditions and process the biological data (*vide infra*). The J_{max} computed in the absence of DA is 12.382 ± 2.036 μA mm^{-2}. Assuming that all the H_2O_2 molecules produced from GLC oxidation at GOx is detected *via* a 2-electron oxidation (Katsounaros et al., 2012), this corresponds to an apparent enzymatic activity of 7.7×10^{13} GLC molecules oxidized per second, per mm^{-2} of electrode surface.

To investigate potential sensing interactions with DA, calibrations (n = 4 electrodes) were repeated in the presence of 5 μM DA (Fig. 6.B, blue line). A similar calibration curve can be observed, but with lower J_{max} and K. This hints at lower GOx activity in the presence of DA, possibly because of DA fouling the enzymes. Oxidized DA is indeed known for binding to thiol-moieties (Zucca et al., 2004; Harreither et al., 2016), which could account for the lower electrode response. Interestingly, the calibration curves are not strongly changed over the 0–5 mM GLC range, which is the one covered during the cell experiments. Therefore, the DA dependence on GLC sensing was not taken into account for the biological tests.

3.5. DA calibration

Even though the GLC PBE sensors were coated with the GOx ink, the enzymes are entrapped in a PEG-DE hydrogel that allows diffusion. Therefore, the possibility to detect DA with the underlying CNT structure was investigated.

CVs carried out in increasing [DA] samples with a complete GLC PBE sensor reveal that the electrode is also sensitive to DA (Fig. 6.C). As for GLC, several features are altered as [DA] increases, but the current recorded at the positive vertex was found to be the most reliable and sensitive.

The calibration data from 4 electrodes was averaged and is presented in Fig. 6.D. As for GLC, a saturation behavior is observed. This is usually attributed to the surface dependence of DA and has been modeled with a Langmuir isotherm (Bath et al., 2000). This model describes the adsorption equilibrium of molecules onto a surface. Here, as DA interacts strongly with the carbon surface, DA adsorption is required to initiate the reaction and is therefore suitably simulated with a Langmuir isotherm (Trouillon and Gijs, 2023). Furthermore, the equation of the Langmuir isotherm can be written as $\theta = \frac{c}{c+K}$, where θ is the surface coverage, c the concentration and K a constant, and is similar to the Michaelis–Menten model. For this reason, the DA calibration data was fit with Eq. (2). Repeating these experiments in the presence of GLC lead to a slight loss in sensitivity, especially for higher [DA] but the impact on the fitting parameters is limited (Table 2).

Finally, PBE sensors without the GOx ink (*i.e.* CNT layers decorated with Pt NP) were also considered for DA detection. Indeed, as the same marker (the current at the positive vertex) is used for both DA and GLC sensing, using sensors without GOx was considered to confirm the DA concentration. Here too, a clear increase in anodic current at 0.9 V is observed (Fig. 6.E) resulting in a saturating calibration curve. Interestingly, repeating these experiments in the presence of 5 mM GLC led to a 30% drop in DA anodic current (Fig. 6.F). This largely due to a drop in J_{max} while K is largely unchanged. This hints that the presence of glucose may hinder DA diffusion because of an increase in viscosity, which could be have a significant impact in this porous material where mass transport is hindered by tortuosity (Marcisz et al., 2020). As the devices were calibrated with the PEG-DE layer, this hindrance is taken into account, and distorted diffusion due to the hydrogel should not impact the measurements.

3.6. DA and GLC dual calibration

Finally, these individual calibration curves for DA and GLC where extended by calibrating the GOx-modified sensors for both GLC and DA, simultaneously, as shown in Fig. 6.G, and for the PBE sensors with and without the GOx ink for the DA calibration (Figure S3). The experimental values where fit with a polynomial regression in Python. As before, the currents recorded for [GLC] = [DA] = 0 mM were subtracted from the data. However, it was found experimentally that this approach is difficult with PBE. Indeed, PBE are fragile and the large number of calibration experiments required is likely to break the paper device before the end of the experiment. Several PBE must therefore used which increases the data variability. Furthermore, the expected currents for DA and GLC are different by about one order of magnitude. The consequence was that this 2-dimensional calibration was not robust for this specific type of device, and another method should be chosen.

Instead, and based on the individual calibration data, it was found that each calibration does depend significantly on the concentration of the other molecule, especially in the linear section of the Michaelis–Menten curve. Hence, it is assumed that each calibration can be taken independently, and that the data shown in Table 2 can be used for biological sensing. The only situation where this does not hold is when DA is detected on PBE without GOx in the presence of glucose. However, during the cell experiments, [GLC] is expected to be close to 5 mM and its impact on the DA calibration is low.

3.7. PC12 cell measurements

As detailed above, 0.5 million PC12 cells were deposited in a gel from the ECM onto the PBE. As shown in Fig. 7.A, the cells, marked with phalloidin (actin cytoskeleton, green) and Sytox (nucleus, red) can be seen in different layers of the z-stack acquired in the paper (inverted DIC, blue). Importantly, it can be observed that the cells are maintained in the ECM gel in the pores of the paper, between the cellulose fibers. This confirms that a 3D cellular model has been built and is cultured in the bulk of the porous PBE.

To investigate the chemical activity of PC12 cells with PBE, we considered 3 different conditions: a control condition, ACh stimulation, and Ach stimulation with pre-incubation with L-DOPA. The protocol can be summarized as:

- The active part of the electrode was dipped into a warm solution of 5 mM glucose (GLC) in PBS during 5 min before electrochemical detection. This is used to equilibrate the GLC concentration in the device

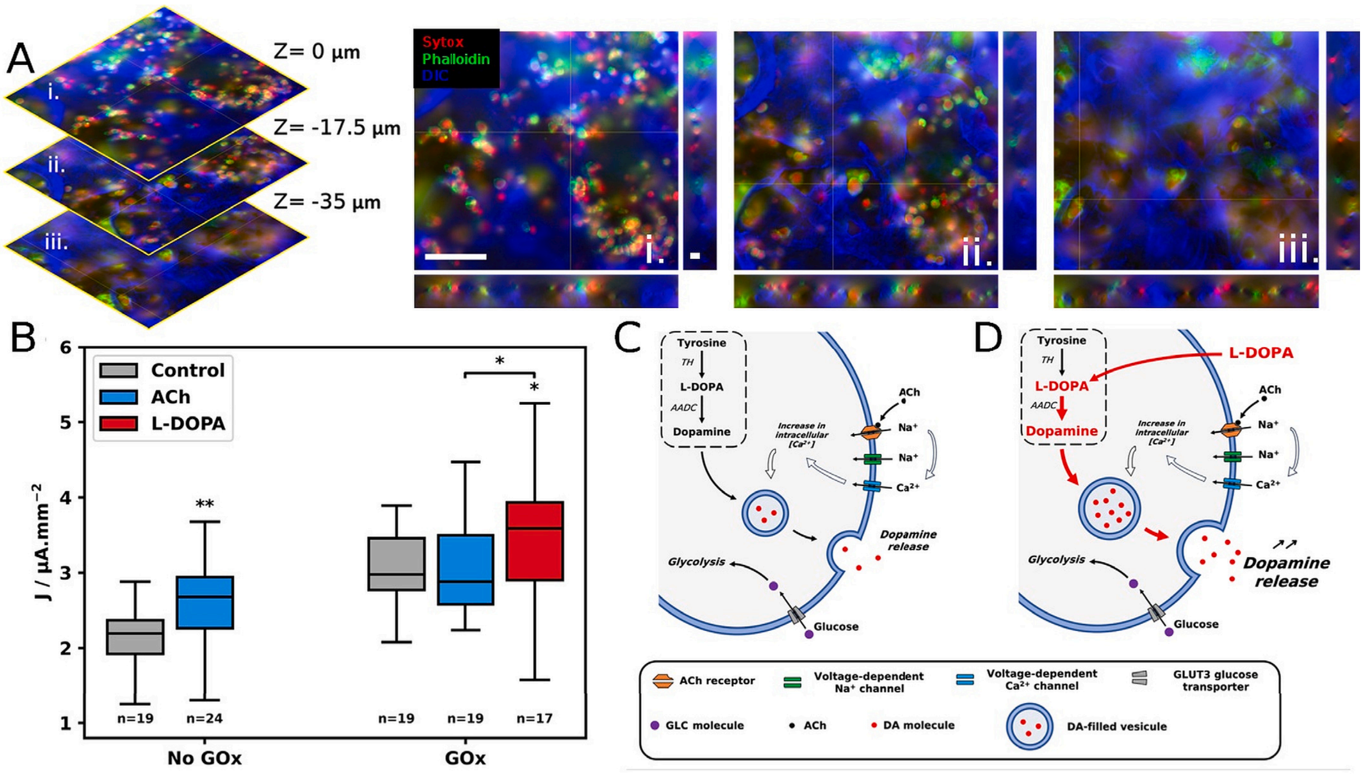

Fig. 7. Cells experiments. (A) Fluorescence images of different slices of a z-stack. The scale bar shows 100 µm in the xy slices and 20 µm in the yz and xz slices. The contrast was adjusted to allow for better observation of the cells (actin in green, nucleus in red) in the pores of the paper (DIC). (B) Current density J after a 200-s incubation in 5 mM GLC in PBS (control condition) or in 5 mM GLC in PBS with 100 µM ACh, without (ACh condition) or with a 1 h-hour preincubation in 100 µM L-DOPA (L-DOPA condition). The data obtained with a CNT and Pt NP PBE, without the GOx ink, are presented on the left, and with a complete GOx PBE device on the right (*: p<0.05, **: p<0.01, ***: p<0.001). Schematic of DA secretion and GLC consumption in PC12 cells (C) in normal conditions and (D) in the presence of L-DOPA.

- The electrode is then dipped into a fresh solution of 5 mM GLC in PBS and connected to the potentiostat
- A first CV is run in a solution of 5 mM GLC in PBS to control the activity of the paper-based sensor.
- Then, the electrode is maintained during 200 s either in a second sample of 5 mM of GLC in PBS (control condition), or in a solution of 100 µM Ach in 5 mM GLC in PBS (cell stimulation). During this step, the devices are kept in the humid incubator.
- Finally, a second CV is run after the 200 s incubation time, which will be analyzed to quantify the GLC consumption and the DA secretion in the neuron-like cell model by comparing it to the first CV.

The L-DOPA conditions followed the same protocol than for the ACh-stimulated condition, but with a 1-h pre-incubation in cell medium with 100 µM of L-DOPA, in the incubator.

CV was chosen for this experimental design, in contrast to amperometry, because of its higher chemical resolution, allowing for clearly identifying features of interest, and thus limiting the risks of chemical interferences. Amperometric assays are typically critical when high time resolution is required. Here, the typical time scale of the events considered is tens of seconds, and compatible with voltammetric measurements. It also allowed for faster and parallel measurements, especially as baseline stabilization is less of a concern with CV than with amperometry. The differential measurement between two sets of CVs allows for taking into account the chemical background of the sample and limiting the risk of measuring interferent molecules at the 0.9 V vertex.

As the complete PBE devices, with the GOx layer, are sensitive to GLC and DA, it is difficult to separate the DA and GLC signals. Consequently, PBE made with only CNT decorated with Pt NP (the 'no GOx' electrode) were used to obtain the DA signal only.

As presented in Fig. 7.B, when the cells cultured on the 'no GOx' electrodes are exposed to ACh, an increase in J is recorded *vs.* the control case ($p < 0.01$). PC12 are dopaminergic cells and this increase in current is therefore attributed to DA release leading to a rise in the DA anodic current. A calibration curve similar to the one shown in Fig. 6.D was computed from CVs recorded with 'no GOx' electrodes in which 2 µl of ECM gel were deposited to account for the distorted mass transport in the gel. From this modified calibration curve, the increase ΔJ in current density was associated to a secreted [DA] of 7.125 µM following exposure to 100 µM ACh, as reported in Table 3. In a similar design (Trouillon and Gijs, 2023), a higher [DA] of 16 µM was found for PC12 cells following ACh stimulation. However, differences in the protocol, for instance the density of the ECM gel, can account for these variations.

However, when the same experiment is repeated with the GOx-modified PBE, and in contrast to the previous result, exposure to ACh decreases slightly J *vs.* the control case. Assuming that the cells behave similarly and secrete the same amount of DA as for the 'no GOx' case, the absence of an overall rise in J could be attributed to a decrease in the GLC current after exposure to ACh. Indeed, the total variation in J can be written as the sum of the changes in DA and GLC current densities:

$$\Delta J_{tot} = \Delta J_{DA} + \Delta J_{GLC} \tag{3}$$

If the cells release 7.125 µM DA, using the data for the GOx PBE calibration, the contribution of DA to the overall change in J can be calculated. As described in Eq. (3), this allows for the computation of the current associated to GLC, and therefore the variations in GLC. Here, it was found that [GLC] drops by 1.149 mM following exposure to ACh.

Physiological [ACh] can vary greatly between the intravesicular, cytoplasmic and extracellular concentrations. Vesicular [ACh] can be

Table 3
Current density variation for the stimulated PC12 cells with ACh, with or without preincubation in 100 μM L-DOPA. The corresponding changes in concentrations were computed from these medians using the calibration data shown in Table 2.

[L-DOPA]/μM		0	100
$\Delta J/\mu A\ mm^{-2}$	GOx	−0.095	0.611*
	No GOx	0.486	
Concentration	$\Delta DA/\mu M$	7.125	20.205
	$\Delta GLC/mM$	−1.149	

Data sets for the 0 μM and 100 μM L-DOPA conditions were tested with a Mann–Whitney U test (*:p<0.05).

10^4 to 10^5 greater than in the cytoplasm (Reimer, 2009). As predicted from osmotic limits, vesicular [ACh] should approach 150 mM, but measurement suggest that it is likely five-fold larger than the predicted concentration (Reimer, 2009). Extracellular [ACh] measurements are more challenging and as it can be few nM, depending of the measurement technique used (Lamy et al., 2021).

In this proof-of-concept assay, ACh is used to stimulate PC12 cells. The concentration chosen for stimulation is therefore very high (probably over physiological levels) to ensure that all the PC12 cells in the samples are stimulated, without [ACh] being a limiting factor in the reaction studied. Furthermore, a 100-μM Ach concentration was chosen because it has been used by other researchers and was reported to induce a maximal level of exocytosis for the study of DA detection (Shinohara et al., 2008).

3.8. Impact of L-DOPA

L-DOPA is the precursor of DA, as presented in Fig. 7.C and 7.D, and is used to artificially increase DA concentration and secretion in neurons (Yu et al., 2024; Trouillon and Gijs, 2023). This strategy is typically used to alleviate the symptoms of Parkinson's disease (Jenner, 2008). In PC12 dopaminergic cells, L-DOPA treatment rapidly increases DA levels in the cytosol >100-fold (Mosharov et al., 2009, 2006). Moreover, L-DOPA treatments is associated with increased DA vesicle size. Incubation of PC12 cells with 20 μM of L-DOPA during only 30 min increased the amount of DA molecules secreted by individual vesicles in DA neurons from 3,000 to 10,600 DA molecules (Pothos et al., 1998), which is in agreement with the data reported here. L-DOPA does not raise the frequency of vesicular exocytosis but increases the average size by at least 250% after incubation with 50 μM of L-DOPA during 1 h (Pothos et al., 1996). The exocytotic mechanisms in the presence of L-DOPA are summarized in Fig. 7.D.

To the best of our knowledge, L-DOPA has no rapid effect on GLC consumption in neurons over time scales comparable to the duration (~1 hour) of the experiments in this study (Zhong et al., 2014; Dai et al., 2023). GLC consumption and therefore ΔJ_{GLC} are considered to be the same between the ACh and L-DOPA conditions while L-DOPA increases DA production by PC12 cells. Therefore, the differences between the ACh and L-DOPA conditions are attributed to changes in DA release only.

For the GOx electrode, an increase in J is indeed observed with 100 μM L-DOPA. Assuming that the drop in glucose concentration is the same, and that a linear assumption can be established for the calibration curves, this rise in J can be attributed to a higher DA concentration of 20.205 μM, about 2.8 the amount detected in the absence of L-DOPA. A higher [DA] after incubation with L-DOPA was previously observed with another PBE, about twice the value recorded without L-DOPA (Trouillon and Gijs, 2016).

3.9. DA secretion and GLC metabolism

Overall, the data obtained from the PBE indicates that DA secretion is associated to an important drop in [GLC]. GLC homeostasis in the brain is critical to regulate the functions of different parts of the brain and allow for neuronal activity (Nimgampalle et al., 2021). This can be explained as an increased metabolic demand during exocytosis following exposure to ACh (Fig. 7.C). In the presence of ACh, several ion transporters decorating the cell membranes are open, thus initiating the exocytotic cascade. Intracellular vesicles are translocated to the cell surface and fuse with its membrane to release their cargo. Energy, and therefore glucose, is used to maintain the electrochemical gradients across the cell membrane and to power the intracellular machinery regulating the vesicle cycle. This leads to a drop in glucose concentration, especially as the concentration of stimulating ACh is here high and will maintain a high level of secretion.

Interestingly, this order of magnitude in [GLC] drop following neuronal or secretory activity was found in humans during cortical spreading depolarization. During these massive depolarization events, the local [GLC] was found to drop by up to 0.5 mM (Rogers et al., 2017). Here, in PBE, as GLC delivery is only passive in the absence of vasculature and because of the slower diffusion in the ECM gel, the drop in GLC is more important. However, the overall behavior of the sample agrees with the chemical events occurring during cortical spreading depolarizations.

4. Conclusion

The co-detection of GLC consumption and DA secretion in neurons model was investigated with paper-based electrode. First, the electrode composition was characterized by XPS and SEM analysis. Four different Pt deposition process were investigated. A three multi-step deposition with 50 cycles was determined to optimize Pt NP deposition on electrode surface. Next, detection of GLC, DA and both molecules were investigated with CV to obtain a calibration curve linking variation in current density to DA and GLC concentration.

Finally, GLC and DA were detected in ACh-activated dopaminergic PC12 cells. DA secretion was confirmed by stimulating the PC12 with the dopamine precursor L-DOPA, leading to a 200% increase in DA secretion as previously observed (Trouillon and Gijs, 2016). Importantly, this was combined to a strong GLC uptake, highlighting the metabolic cost of secretion. The concentration of ACh used here is high, and the level of cell stimulation is expected to be beyond the physiological range, but this result hints at the possibility of using a paper-based electrode for investigating the metabolic cost of the brain activity. Beyond the technical advancement of the field of paper devices, brain metabolism is still largely not understood because of the complexity of that organ. Culture of neurons on paper chips has already been reported (Dermutz et al., 2017; Aebersold et al., 2018), and the possibility to build implantable, tissue-like structures has been described (Cramer et al., 2019). Primary cells and homogenized tissues could also be used as cell stock for artificial tissue culture on paper. The possibility to quantify in large datasets the chemical inputs and outputs of brain mechanisms will help us understanding better the causes of brain pathologies related to glucose uptake or metabolism, and proposing new therapeutic strategies.

CRediT authorship contribution statement

Rémi F. Dutheil: Writing – review & editing, Writing – original draft, Software, Methodology, Investigation, Formal analysis, Data curation. **Dabeaurard Tho:** Methodology, Investigation. **Iman Pitroipa:** Methodology, Investigation. **Raphaël Trouillon:** Writing – review & editing, Writing – original draft, Validation, Supervision, Resources, Project administration, Methodology, Investigation, Funding acquisition, Conceptualization.

Funding sources

This research was funded by the TransMedTech Institute, the Ecole Polytechnique de Montréal, the FNFR grant number NFRFE-2022-00671, the NSERC grant number RGPIN-2023-05437 and the FRQNT grant number 312011.

Declaration of competing interest

The authors declare the following financial interests/personal relationships which may be considered as potential competing interests: Raphael Trouillon reports financial support was provided by TransMedTech Institute. Raphael Trouillon reports financial support was provided by Polytechnique Montreal. Raphael Trouillon reports financial support was provided by FNFR. Raphael Trouillon reports financial support was provided by Natural Sciences and Engineering Research Council of Canada. Raphael Trouillon reports financial support was provided by Quebec Research Fund Nature and Technology. If there are other authors, they declare that they have no known competing financial interests or personal relationships that could have appeared to influence the work reported in this paper.

Acknowledgments

We thank Ms. Edith Mariez and Mr. Oscar Joaquin Isasmendi Ramirez for their help with Python analysis, and Ms. Juliette Pelletier for assisting with the SEM images. The authors acknowledge Dr. Chris Law at Concordia University, Canada's Centre for Microscopy and Cellular Imaging (CMCI) and Josianne Lefebvre at Polytechnique Montreal's LASM.

Appendix A. Supplementary data

Supplementary material related to this article can be found online at https://doi.org/10.1016/j.biosx.2025.100601.

Data availability

Data will be made available on request.

References

Adams, R.N., 1976. Probing brain chemistry with electroanalytical techniques. Anal. Chem. 48 (14), 1126A–1138A.

Aebersold, M.J., Thompson-Steckel, G., Joutang, A., Schneider, M., Burchert, C., Forró, C., Weydert, S., Han, H., Vörös, J., 2018. Simple and inexpensive paper-based astrocyte co-culture to improve survival of low-density neuronal networks. Front. Neurosci. 12, URL https://www.frontiersin.org/articles/10.3389/fnins.2018.00094.

Ali, S.H., Trouillon, R., 2024. Paper Sensors for the measurement of nitric oxide release from endothelial cells. Sensors Diagn. URL https://pubs.rsc.org/en/content/articlehtml/2024/sd/d4sd00154k, Publisher: Royal Society of Chemistry.

Bai, Y., Yang, W., Sun, Y., Sun, C., 2008. Enzyme-free glucose sensor based on a three-dimensional gold film electrode. Sensors Actuators B: Chem. 134 (2), 471–476.

Bankar, S.B., Bule, M.V., Singhal, R.S., Ananthanarayan, L., 2009. Glucose oxidase — An overview. Biotech. Adv. 27 (4), 489–501. http://dx.doi.org/10.1016/j.biotechadv.2009.04.003, URL https://www.sciencedirect.com/science/article/pii/S0734975009000536.

Bard, A.J., Faulkner, L.R., White, H.S., 2022. Electrochemical Methods: Fundamentals and Applications. John Wiley & Sons.

Bath, B.D., Michael, D.J., Trafton, B.J., Joseph, J.D., Runnels, P.L., Wightman, R.M., 2000. Subsecond adsorption and desorption of dopamine at carbon-fiber microelectrodes. Anal. Chem. 72 (24), 5994–6002.

Bertoncello, P., Edgeworth, J.P., Macpherson, J.V., Unwin, P.R., 2007. Trace level cyclic voltammetry facilitated by single-walled carbon nanotube network electrodes. J. Am. Chem. Soc. 129 (36), 10982–10983.

Bouffier, L., Zigah, D., Sojic, N., Kuhn, A., 2021. Bipolar (bio) electroanalysis. Annu. Rev. Anal. Chem. 14, 65–86.

Bruzewicz, D.A., Reches, M., Whitesides, G.M., 2008. Low-cost printing of poly (dimethylsiloxane) barriers to define microchannels in paper. Anal. Chem. 80 (9), 3387–3392.

Carlsson, A., Lindqvist, M., Magnusson, T., 1957. 3, 4-Dihydroxyphenylalanine and 5-hydroxytryptophan as reserpine antagonists. Nature 180 (4596), 1200.

Carlsson, A., Lindqvist, M., Magnusson, T., Waldeck, B., 1958. On the presence of 3-hydroxytyramine in brain. Science 127 (3296), 471.

Cate, D.M., Adkins, J.A., Mettakoonpitak, J., Henry, C.S., 2015. Recent developments in paper-based microfluidic devices. Anal. Chem. 87 (1), 19–41.

Cramer, S.M., Larson, T.S., Lockett, M.R., 2019. Tissue papers: Leveraging paper-based microfluidics for the next generation of 3D tissue models. Anal. Chem. 91 (17), 10916–10926. http://dx.doi.org/10.1021/acs.analchem.9b02102, Publisher: American Chemical Society.

Dai, C., Tan, C., Zhao, L., Liang, Y., Liu, G., Liu, H., Zhong, Y., Liu, Z., Mo, L., Liu, X., et al., 2023. Glucose metabolism impairment in Parkinson's disease. Brain Res. Bull. 199, 110672.

Derda, R., Laromaine, A., Mammoto, A., Tang, S.K., Mammoto, T., Ingber, D.E., Whitesides, G.M., 2009. Supported 3D cell culture for tissue-based bioassays. Proc. Natl. Acad. Sci. 106 (44), 18457–18462.

Dermutz, H., Thompson-Steckel, G., Forró, C., Lange, V.d., Dorwling-Carter, L., Vörös, J., Demkó, L., 2017. Paper-based patterned 3D neural cultures as a tool to study network activity on multielectrode arrays. RSC Adv. 7 (62), 39359–39371. http://dx.doi.org/10.1039/C7RA00971B, URL https://pubs.rsc.org/en/content/articlelanding/2017/ra/c7ra00971b, Publisher: The Royal Society of Chemistry.

Dienel, G.A., 2019. Brain glucose metabolism: integration of energetics with function. Physiol. Rev. 99 (1), 949–1045.

Dossi, N., Toniolo, R., Piccin, E., Susmel, S., Pizzariello, A., Bontempelli, G., 2013. Pencil-drawn dual electrode detectors to discriminate between analytes comigrating on paper-based fluidic devices but undergoing electrochemical processes with different reversibility. Electroanalysis 25 (11), 2515–2522.

Gooding, J.J., 2005. Nanostructuring electrodes with carbon nanotubes: A review on electrochemistry and applications for sensing. Electrochim. Acta 50 (15), 3049–3060.

Han, R., Liang, J., Zhou, B., 2021. Glucose metabolic dysfunction in neurodegenerative diseases—new mechanistic insights and han2021glucosethe potential of hypoxia as a prospective therapy targeting metabolic reprogramming. Int. J. Mol. Sci. 22 (11), 5887.

Harreither, W., Trouillon, R., Poulin, P., Neri, W., Ewing, A.G., Safina, G., 2016. Cysteine residues reduce the severity of dopamine electrochemical fouling. Electrochim. Acta 210, 622–629.

Hyman, S.E., 2005. Neurotransmitters. Curr. Biol. 15 (5), R154–R158.

Jalloh, I., Carpenter, K.L., Helmy, A., Carpenter, T.A., Menon, D.K., Hutchinson, P.J., 2015. Glucose metabolism following human traumatic brain injury: methods of assessment and pathophysiological findings. Metab. Brain Dis. 30, 615–632.

Jenner, P., 2008. Molecular mechanisms of L-DOPA-induced dyskinesia. Nature Rev. Neurosci. 9 (9), 665–677.

Johnson, K.A., Goody, R.S., 2011. The original Michaelis constant: translation of the 1913 Michaelis–Menten paper. Biochemistry 50 (39), 8264–8269.

Katsounaros, I., Schneider, W.B., Meier, J.C., Benedikt, U., Biedermann, P.U., Auer, A.A., Mayrhofer, K.J.J., 2012. Hydrogen peroxide electrochemistry on platinum: towards understanding the oxygen reduction reaction mechanism. Phys. Chem. Chem. Phys. 14 (20), 7384–7391. http://dx.doi.org/10.1039/C2CP40616K, URL https://pubs.rsc.org/en/content/articlelanding/2012/cp/c2cp40616k, Publisher: The Royal Society of Chemistry.

Khatami, S.H., Vakili, O., Ahmadi, N., Soltani Fard, E., Mousavi, P., Khalvati, B., Maleksabet, A., Savardashtaki, A., Taheri-Anganeh, M., Movahedpour, A., 2022. Glucose oxidase: Applications, sources, and recombinant production. Biotechnol. Appl. Biochem. 69 (3), 939–950. http://dx.doi.org/10.1002/bab.2165, URL https://onlinelibrary.wiley.com/doi/abs/10.1002/bab.2165, _eprint: https://onlinelibrary.wiley.com/doi/pdf/10.1002/bab.2165.

Knudsen, J.R., Persson, K.W., Henriquez-Olguin, C., Li, Z., Di Leo, N., Hesselager, S.A., Raun, S.H., Hingst, J.R., Trouillon, R., Wohlwend, M., et al., 2023. Microtubule-mediated GLUT4 trafficking is disrupted in insulin-resistant skeletal muscle. Elife 12, e83338.

Lamy, E., Pilyser, L., Paquet, C., Bouaziz-Amar, E., Grassin-Delyle, S., 2021. High-sensitivity quantification of acetylcholine and choline in human cerebrospinal fluid with a validated LC-MS/MS method. Talanta 224, 121881. http://dx.doi.org/10.1016/j.talanta.2020.121881, URL https://www.sciencedirect.com/science/article/pii/S0039914020311723.

Lee, W.-C., Kim, K.-B., Gurudatt, N., Hussain, K.K., Choi, C.S., Park, D.-S., Shim, Y.-B., 2019. Comparison of enzymatic and non-enzymatic glucose sensors based on hierarchical au-Ni alloy with conductive polymer. Biosens. Bioelectron. 130, 48–54.

Liu, S., Su, W., Ding, X., 2016. A review on microfluidic paper-based analytical devices for glucose detection. Sensors 16 (12), 2086.

Mandpe, P., Prabhakar, B., Gupta, H., Shende, P., 2020. Glucose oxidase-based biosensor for glucose detection from biological fluids. Sensor Rev. 40 (4), 497–511. http://dx.doi.org/10.1108/SR-01-2019-0017, URL https://www.emerald.com/insight/content/doi/10.1108/sr-01-2019-0017/full/html, Publisher: Emerald Publishing Limited.

Marcisz, K., Kaniewska, K., Karbarz, M., 2020. Smart functionalized thin gel layers for electrochemical sensors, biosensors and devices. Curr. Opin. Electrochem. 23, 57–64. http://dx.doi.org/10.1016/j.coelec.2020.03.011, URL https://www.sciencedirect.com/science/article/pii/S2451910320300685, Electrocatalysis Sensors and Biosensors.

Marsden, C.A., 2006. Dopamine: the rewarding years. Br. J. Pharmacol. 147 (S1), S136–S144.

Martinez, A.W., Phillips, S.T., Butte, M.J., Whitesides, G.M., 2007. Patterned paper as a platform for inexpensive, low-volume, portable bioassays. Angew. Chem. 119 (8), 1340–1342.

Michael, A.C., Borland, L., 2006. Electrochemical Methods for Neuroscience. CRC Press.

Michaelis, L., Menten, M.L., et al., 1913. Die kinetik der invertinwirkung. Biochem. Z. 49 (333–369), 352.

Mosharov, E.V., Larsen, K.E., Kanter, E., Phillips, K.A., Wilson, K., Schmitz, Y., Krantz, D.E., Kobayashi, K., Edwards, R.H., Sulzer, D., 2009. Interplay between cytosolic dopamine, calcium, and α-synuclein causes selective death of substantia nigra neurons. Neuron 62 (2), 218–229.

Mosharov, E.V., Staal, R.G., Bové, J., Prou, D., Hananiya, A., Markov, D., Poulsen, N., Larsen, K.E., Moore, C.M., Troyer, M.D., et al., 2006. α-Synuclein overexpression increases cytosolic catecholamine concentration. J. Neurosci. 26 (36), 9304–9311.

Neubauerova, K., Carneiro, M.C., Rodrigues, L.R., Moreira, F.T., Sales, M.G.F., 2020. Nanocellulose-based biosensor for colorimetric detection of glucose. Sens. Bio Sens. Res. 29, 100368.

Nimgampalle, M., Chakravarthy, H., Devanathan, V., 2021. Chapter 8 - glucose metabolism in the brain: An update. In: Viswanath, B. (Ed.), Recent Developments in Applied Microbiology and Biochemistry. Academic Press, pp. 77–88. http://dx.doi.org/10.1016/B978-0-12-821406-0.00008-4, URL https://www.sciencedirect.com/science/article/pii/B9780128214060000084.

Ozer, T., McMahon, C., Henry, C.S., 2020. Advances in paper-based analytical devices. Annu. Rev. Anal. Chem. 13 (1), 85–109.

Pelletier, J., Trouillon, R., 2024. Tuning the properties of paper-based electrodes for neurochemical analysis. Electrochim. Acta 475, 143528.

Pothos, E.N., Davila, V., Sulzer, D., 1998. Presynaptic recording of quanta from midbrain dopamine neurons and modulation of the quantal size. J. Neurosci. 18 (11), 4106–4118.

Pothos, E., Desmond, M., Sulzer, D., 1996. L-3, 4-dihydroxyphenylalanine increases the quantal size of exocytotic dopamine release in vitro. J. Neurochem. 66 (2), 629–636.

Pumera, M., 2009. The electrochemistry of carbon nanotubes: fundamentals and applications. Chem. Eur. J. 15 (20), 4970–4978.

Raj, C.R., Okajima, T., Ohsaka, T., 2003. Gold nanoparticle arrays for the voltammetric sensing of dopamine. J. Electroanal. Chem. 543 (2), 127–133.

Reimer, R., 2009. Vesicular neurotransmitter transporters. In: Squire, L.R. (Ed.), Encyclopedia of Neuroscience. Academic Press, Oxford, pp. 107–113. http://dx.doi.org/10.1016/B978-008045046-9.01356-5, URL https://www.sciencedirect.com/science/article/pii/B9780080450469013565.

Rogers, M.L., Feuerstein, D., Leong, C.L., Takagaki, M., Niu, X., Graf, R., Boutelle, M.G., 2013. Continuous online microdialysis using microfluidic sensors: dynamic neurometabolic changes during spreading depolarization. ACS Chem. Neurosci. 4 (5), 799–807.

Rogers, M.L., Leong, C.L., Gowers, S.A., Samper, I.C., Jewell, S.L., Khan, A., McCarthy, L., Pahl, C., Tolias, C.M., Walsh, D.C., et al., 2017. Simultaneous monitoring of potassium, glucose and lactate during spreading depolarization in the injured human brain–proof of principle of a novel real-time neurochemical analysis system, continuous online microdialysis. J. Cereb. Blood Flow Metab. 37 (5), 1883–1895.

Schneider, C.A., Rasband, W.S., Eliceiri, K.W., 2012. NIH image to ImageJ: 25 years of image analysis. Nature Methods 9 (7), 671–675.

Scholz, F., et al., 2010. Electroanalytical Methods, vol. 1, Springer.

Shinohara, H., Wang, F., Hossain, S.M.Z., 2008. A convenient, high-throughput method for enzyme-luminescence detection of dopamine released from PC12 cells. Nat. Protoc. 3 (10), 1639–1644. http://dx.doi.org/10.1038/nprot.2008.158, URL https://www.nature.com/articles/nprot.2008.158, Publisher: Nature Publishing Group.

Simonsson, L., Kurczy, M.E., Trouillon, R., Hook, F., Cans, A.-S., 2012. A functioning artificial secretory cell. Sci. Rep. 2 (1), 824.

Smith, S.K., Lugo-Morales, L.Z., Tang, C., Gosrani, S.P., Lee, C.A., Roberts, J.G., Morton, S.W., McCarty, G.S., Khan, S.A., Sombers, L.A., 2018. Quantitative comparison of enzyme immobilization strategies for glucose biosensing in real-time using fast-scan cyclic voltammetry coupled with carbon-fiber microelectrodes. ChemPhysChem 19 (10), 1197–1204.

Sun, K., Yang, Y., Zhou, H., Yin, S., Qin, W., Yu, J., Chiu, D.T., Yuan, Z., Zhang, X., Wu, C., 2018. Ultrabright polymer-dot transducer enabled wireless glucose monitoring via a smartphone. ACS Nano 12 (6), 5176–5184.

Taguchi, T., Miwa, I., Mizutani, T., Nakajima, H., Fukumura, Y., Kobayashi, I., Yabuuchi, M., Miwa, I., 2003. Determination of D-mannose in plasma by HPLC. Clin. Chem. 49 (1), 181–183.

Trouillon, R., Cheung, C., Patel, B.A., O'Hare, D., 2010. Electrochemical study of the intracellular transduction of vascular endothelial growth factor induced nitric oxide synthase activity using a multi-channel biocompatible microelectrode array. Biochim. et Biophys. Acta (BBA)- Gen. Subj. 1800 (9), 929–936.

Trouillon, R., Gijs, M.A., 2016. Dynamic electrochemical quantitation of dopamine release from a cells-on-paper system. RSC Adv. 6 (37), 31069–31073.

Trouillon, R., Gijs, M.A., 2018. Paper-based polymer electrodes for bioanalysis and electrochemistry of neurotransmitters. ChemPhysChem 19 (10), 1164–1172.

Trouillon, R., Gijs, M.A., 2023. Cells-on-electrode-on-paper: Analytical platforms for the chemical study of cellular secretion. Biosens. Bioelectronics: X 14, 100327.

Trouillon, R., Letizia, M.C., Menzies, K.J., Mouchiroud, L., Auwerx, J., Schoonjans, K., Gijs, M.A., 2017. A multiscale study of the role of dynamin in the regulation of glucose uptake. Integr. Biol. 9 (10), 810–819.

Vannucci, R.C., Vannucci, S.J., 2000. Glucose metabolism in the developing brain. Sem. Perinatol. 24 (2), 107–115.

Vasylieva, N., Barnych, B., Meiller, A., Maucler, C., Pollegioni, L., Lin, J.-S., Barbier, D., Marinesco, S., 2011. Covalent enzyme immobilization by poly (ethylene glycol) diglycidyl ether (PEGDE) for microelectrode biosensor preparation. Biosens. Bioelectron. 26 (10), 3993–4000.

Vespa, P.M., McArthur, D., O'Phelan, K., Glenn, T., Etchepare, M., Kelly, D., Bergsneider, M., Martin, N.A., Hovda, D.A., 2003. Persistently low extracellular glucose correlates with poor outcome 6 months after human traumatic brain injury despite a lack of increased lactate: a microdialysis study. J. Cereb. Blood Flow Metab. 23 (7), 865–877.

Wang, J., 2008. Electrochemical glucose biosensors. Chem. Rev. 108 (2), 814–825.

Webster, R., 2001. Neurotransmitters, Drugs and Brain Function. John Wiley & Sons.

Yu, D., Wang, H., Zhai, Y., Lei, Z., Sun, M., Chen, S., Yin, P., Wang, X., 2024. Effects of latroeggtoxin-VI on dopamine and α-synuclein in PC12 cells and the implications for Parkinson's disease. Biol. Res. 57 (1), 9.

Zachek, M.K., Hermans, A., Wightman, R.M., McCarty, G.S., 2008. Electrochemical dopamine detection: Comparing gold and carbon fiber microelectrodes using background subtracted fast scan cyclic voltammetry. J. Electroanal. Chem. 614 (1–2), 113–120.

Zhong, S.-Y., Chen, Y.-X., Fang, M., Zhu, X.-L., Zhao, Y.-X., Liu, X.-Y., 2014. Low-dose levodopa protects nerve cells from oxidative stress and up-regulates expression of pCREB and CD39. PLoS One 9 (4), e95387.

Zimmet, P.Z., Magliano, D.J., Herman, W.H., Shaw, J.E., 2014. Diabetes: a 21st century challenge. Lancet Diabetes Endocrinol. 2 (1), 56–64.

Zucca, F.A., Giaveri, G., Gallorini, M., Albertini, A., Toscani, M., Pezzoli, G., Lucius, R., Wilms, H., Sulzer, D., Ito, S., et al., 2004. The neuromelanin of human substantia Nigra: physiological and pathogenic aspects. Pigment Cell Res. 17 (6), 610–617.